Ultrafast optical stress on $BaFe_2As_2$

Takeshi Suzuki,[1,*] Yuya Kubota,[2,3] Asuka Nakamura,[4,5] Takahiro Shimojima,[4,5] Kou Takubo,[1,†] Suguru Ito,[1,‡] Kohei Yamamoto,[1,§] Shoya Michimae,[1] Hikaru Sato,[6] Hidenori Hiramatsu,[6,7] Hideo Hosono,[7] Tadashi Togashi,[2,3] Makina Yabashi,[2,3] Hiroki Wadati,[1,¶] Iwao Matsuda,[1] Shik Shin,[8,9,**] and Kozo Okazaki[1,9,10,††]

[1]*Institute for Solid State Physics, The University of Tokyo, Kashiwa, Chiba 277-8581, Japan*
[2]*Japan Synchrotron Radiation Research Institute, 1-1-1 Kouto, Sayo, Hyogo 679-5198, Japan*
[3]*RIKEN SPring-8 Center, 1-1-1 Kouto, Sayo, Hyogo 679-5148, Japan*
[4]*RIKEN Center for Emergent Matter Science (CEMS), Wako 351-0198, Japan*
[5]*Quantum-Phase Electronics Center (QPEC) and Department of Applied Physics, The University of Tokyo, Tokyo 113-8656, Japan*
[6]*Laboratory for Materials and Structures, Institute of Innovative Research, Tokyo Institute of Technology, Tokyo 226-8503, Japan*
[7]*Materials Research Center for Element Strategy, Tokyo Institute of Technology, Yokohama 226-8503, Japan*
[8]*Office of University Professor, The University of Tokyo, Kashiwa, Chiba 277-8581 Japan*
[9]*Material Innovation Research Center, The University of Tokyo, Kashiwa, Chiba 277-8561, Japan*
[10]*Trans-scale Quantum Science Institute, The University of Tokyo, Bunkyo-ku, Tokyo 113-0033, Japan*

(Received 12 April 2021; accepted 20 July 2021; published 8 September 2021)

We investigate the ultrafast lattice dynamics in $BaFe_2As_2$ via time-resolved x-ray diffraction measurements using an x-ray free-electron laser at SPring-8 Angstrom Compact free-electron LAser (SACLA). The profile of the Bragg peaks substantially changes after strong photoexcitation, where the c axis length of the lattice initially contracts, followed by expansion. These ultrafast lattice contractions and expansions significantly depend on the pump fluence, and it is suggested that a strong normal stress is applied along the c axis. To obtain a phenomenological understanding of the observed lattice dynamics, we performed calculations based on a two-temperature model and an ultrafast thermoelasticity model. Our results showed that a steep gradient of the electron temperature induced by photoexcitation generates a blast force, which acts as a strong normal stress. We propose that a temporal stress can be applied by a strong optical pump, and this scheme can be another route for the application of uniaxial stress to superconductors.

DOI: 10.1103/PhysRevResearch.3.033222

I. INTRODUCTION

Ultrafast optical pulses have been intensively employed in condensed matter physics to induce numerous exotic states that can never appear under equilibrium [1]. Understanding how the degrees of freedom of charge, lattice, and spin evolve by interacting with each other is the central element for manipulating a material of interest and to eventually develop next-generation devices such as ultrafast quantum memory or highly efficient optical switching. One of the topical and interesting routes is to temporally engineer the lattice structure, by which photo-induced insulating [2], charge density waves [3,4], and superconducting states [5,6] have been reported. The underling mechanisms depend on combinations of materials and profiles of the used optical pulses. For example, photo-induced superconductivities were reported to be achieved by resonantly exciting an infrared active phonon mode, which is then transferred to a Raman active phonon mode that is responsible for superconductivity through nonlinear intermode coupling [7]. Another example is found in displacive excited coherent phonons, which are generated because of the instant change in the minimum position of a free-energy curve in the lattice coordinates, where the initial excitation of the electron system alters the lattice coordinates via electron-phonon couplings [8]. Thus, ultrafast lattice design can be realized by various methods, and various schemes are desired to realize wider and more flexible functionalities.

Regarding quantum materials, iron-based superconductors provide particularly interesting playgrounds not only for their

*takeshi.suzuki@issp.u-tokyo.ac.jp
†Present address: Department of Chemistry, Tokyo Institute of Technology, Tokyo 152-8551, Japan.
‡Present address: Department of Physics, Philipps-University of Marburg, 35032 Marburg, Germany.
§Present address: Institute for Molecular Science, Okazaki, Aichi 444-8585, Japan.
¶Present address: Graduate School of Material Science, University of Hyogo, Koto, Hyogo 678-1297, Japan.
**shin@issp.u-tokyo.ac.jp
††okazaki@issp.u-tokyo.ac.jp

yet unsettled superconducting mechanisms [9–14] but also for exploring exotic electronic properties, such as electronic nematicity [15–17] or crossover from the Bardeen-Cooper-Schrieffer (BCS) regime to the Bose-Einstein condensation regime [18–21]. These intriguing electronic properties emerge through an interplay among the degrees of freedom of charge, spin, and lattice. Therefore, modifications of a pure crystal, such as intercalation of a spacer layer [22] or growth of a single layer [23], can significantly increase the superconducting transition temperature (T_c). Especially for $BaFe_2As_2$, controlling the lattice profile by isovalent substitution [24] or physical pressure [25] substantially alters the electronic properties, resulting in the emergence of superconductivity. In this respect, photoexcitation has a strong advantage over other techniques for ion-based superconductors because it can instantaneously change the physical properties without contact or fabrication. One of the most spectacular phenomena is photo-induced superconductivity, which has also been suggested to be realized in iron-based superconductors measured by time- and angle-resolved photoemission spectroscopy (TARPES) [26,27]. In these studies, the lattice modulation was found to play an important role for realizing superconducting-like states, which strongly motivated us to directly observe the lattice dynamics.

In addition to photo-induced superconductivity, photoexcited phenomena in iron-based superconductors have been intensively studied. The key mechanism is the connection of the electronic and magnetic properties to lattice modulations. In photoexcited FeSe, significant energy shifts of the bands due to the coherent phonons have been reported by TARPES and by time-resolved x-ray diffraction (TRXRD) [28,29]. In photoexcited $BaFe_2As_2$, the temporal periodic formation of spin density waves [30] or chemical potential control [31] synchronized with lattice modulations after photoexcitation have been reported. Thus, direct observations of the lattice dynamics triggered by ultrafast photoexcitation is in high demand to better understand and further explore unknown photo-induced phenomena. Previously, coherent phonons [32] and orthorhombic distortion [33] were reported in $BaFe_2As_2$ by TRXRD. In this work, we are interested in the change of lattice constants and induced stress after strong excitation. For this purpose, x-ray free-electron laser (XFEL) is a very powerful tool because it can provide short pulsed photon flux sources to achieve a time resolution better than the picosecond order [29,34–36].

Here, we studied the ultrafast lattice dynamics of $BaFe_2As_2$ by TRXRD measurements using XFEL at the SPring-8 Angstrom Compact free-electron LAser (SACLA) [37]. We measured the time-dependent diffractions for $(00l)$ and observed the lattice contraction in the direction of the c axis immediately after photoexcitation followed by expansion. These ultrafast lattice contractions and expansions caused by normal stress along the c axis direction significantly depend on the pump fluence. To investigate the mechanisms underlying these dynamics, we performed calculations based on the combined simple models, which comprise a two-temperature model and an ultrafast thermoelasticity model. The initial lattice contraction is due to a strong blast force, which is triggered by the prominent distribution of the electron temperature along the depth direction, whereas the

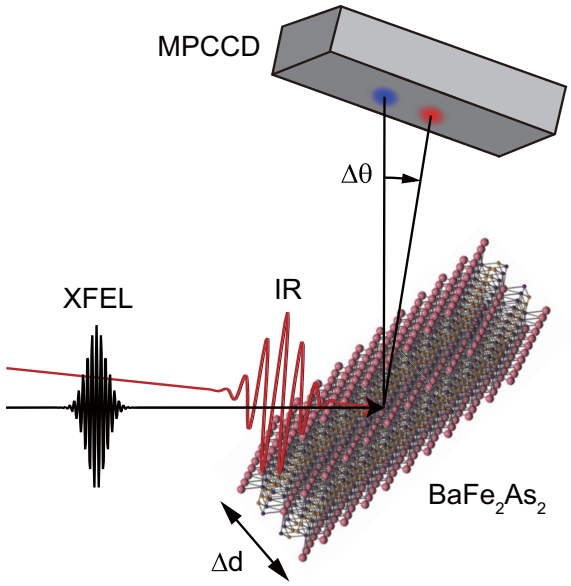

FIG. 1. Schematic diagram of the TRXRD measurements for $BaFe_2As_2$. An infrared (IR) pulse was used for the pump, and a hard x-ray pulse (9.35 keV) obtained from a free-electron laser (FEL), SACLA, was used as a probe to obtain the lattice diffractions from a crystal lattice in a time-resolved manner. A two-dimensional detector MPCCD was used to capture a diffraction image. The sample was deposited on a MgO substrate, and the thickness was 250 nm.

lattice expansion is explained by the energy transfer of the electron to the lattice systems. Furthermore, we showed that a significant distribution of normal stress along the direction of the c axis can be temporarily achieved, in which the normal stress is significantly enhanced near the surface. Although similar phenomena to our finding may be observed for other materials [38], we demonstrate the applicability of ultrafast optical stress on an iron-based superconductor which has a potential to show an enhanced superconductivity under physical pressure. Our results suggest that photoexcitation can be used as an alternative way to apply normal stress on an ultrafast time scale without using static conventional methods.

II. METHOD

Figure 1 shows an illustration of our experimental setup for the TRXRD measurements. TRXRD measurements were implemented as a pump-probe-type experiment, where infrared pulses were used for the pump, whereas hard x-ray pulses of XFEL were used for the probe. All experiments were performed at SACLA BL3. Infrared pump pulses were obtained from the chirped pulse amplification Ti:sapphire laser system with a center wavelength of 800 nm and a time duration of less than 27 fs. For probe pulses, we used XFEL in SACLA BL3, where the time duration is less than 10 fs, and the center photon energy is 9.35 keV [39,40]. Owing to the timing jitter of the XFEL, we typically achieved a time resolution of a few hundred femtoseconds in the pump-probe measurements, which can be improved by ∼30 fs after timing corrections are performed using the arrival-timing monitor technique [41–43]. The available photon flux is on the order

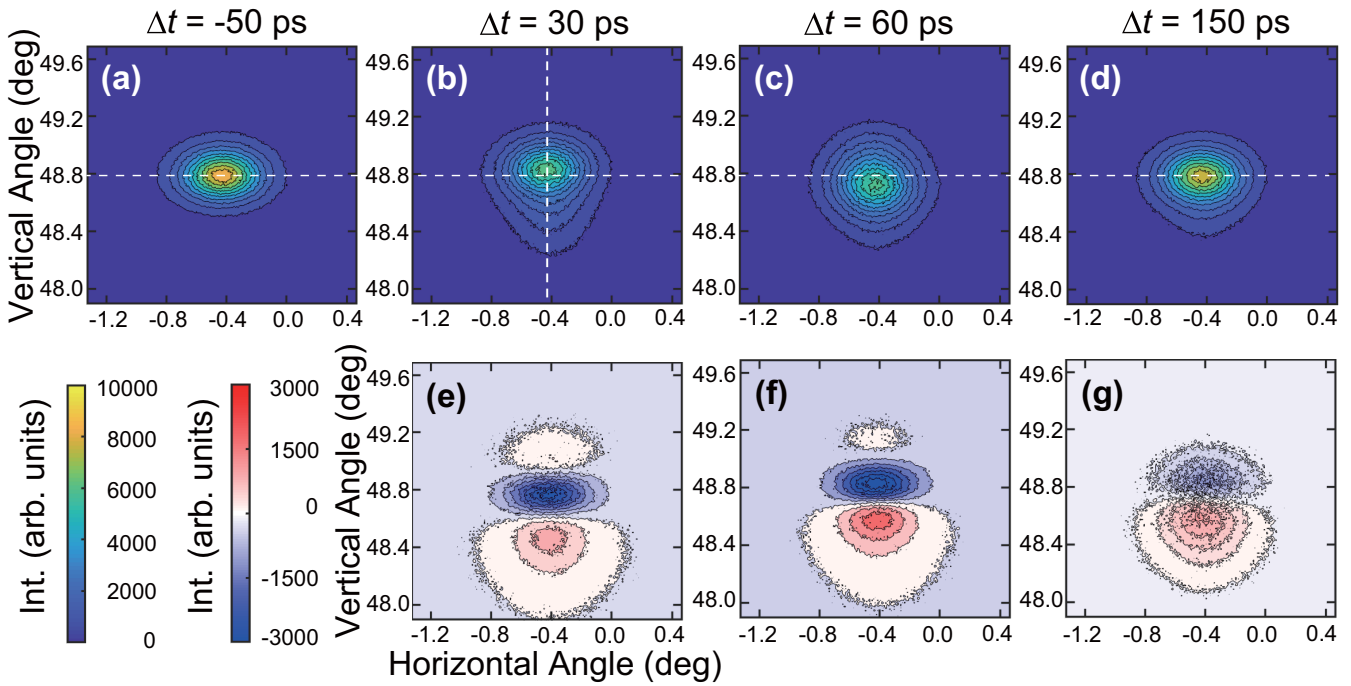

FIG. 2. (a)–(d) TRXRD image around the (008) Bragg peak. The vertical angle is measured with respect to the incoming x-ray beams. The delay time between the pump and the probe, Δt, is indicated in each image. The pump fluence used was 16.7 mJ/cm^2. The horizontal whited-dashed lines correspond to the peak position at $\Delta t = -50$ ps. The vertical dashed-white line at Fig. 2(b) intersects the highest point of the peak. (e)–(g) Difference images were obtained by subtracting the average image before the arrival of the pump. The red and blue colors indicate an increase and decrease, respectively.

of 10^{11} per pulse, which enables us to obtain better signal-to-noise ratio compared with the regular synchrotron with using a slicing technique. For the detector, we used a multiport charge-coupled device (MPCCD) to capture Bragg diffraction peaks in two-dimensional images [44]. The lattice distance, d_{hkl}, between successive crystallographic planes (hkl), is related to the diffraction angle θ_{hkl} by

$$2d_{hkl}\sin\theta_{hkl} = n\lambda, \tag{1}$$

where n is a positive integer and λ is the probed wavelength of the x-ray. From the Bragg condition in Eq. (1), we can obtain the relationship between the pump-induced changes in the lattice distance Δd_{hkl} and the diffraction angle $\Delta\theta_{hkl}$ as

$$\frac{\Delta d_{hkl}}{d_{hkl}} = -\frac{\Delta\theta_{hkl}}{\tan\theta_{hkl}}. \tag{2}$$

In the case of $(hkl) = (00l)$, we can obtain the length change along the c axis as $\Delta d/d = \Delta d_{00l}/d_{00l}$, where we define the length of the unit cell along the c axis as d. When the lattice constant changes, unless the incident angle with respect to the sample is correspondingly changed, Eq. (1) cannot hold, and the diffraction peak should not be observed. However, we could successfully observe the temporal change of the diffraction peak. This should mean that Eq. (1) holds without change of the incident angle for some reason.

Samples of $BaFe_2As_2$ were deposited on a MgO substrate by pulsed laser deposition [45]. The sample thickness was 250 nm. All measurements in this work were performed at room temperature. The lattice parameters in the tetragonal phase for $BaFe_2As_2$ are $a = 3.9625$ Å, $c = 13.0168$ Å [46].

III. RESULTS

Figures 2(a)–2(d) show the TRXRD results for the (008) Bragg peaks at the indicated pump-probe delays (Δt), where the pump fluence is 16.7 mJ/cm^2. The vertical angle is measured with respect to the incoming x-ray beams. As a result, the change of measured peak denoted as $\Delta\theta$ in Fig. 1 is related to the change of the diffraction angle $\Delta\theta_{hkl}$ by $\Delta\theta = 2\Delta\theta_{hkl}$. To further clarify the pump-induced change, we also show the difference spectra in Figs. 2(e)–2(g), in which we have subtracted each spectrum by the reference spectrum averaged before the arrival of the pump. After strong pump excitation, the peak is broadened toward the lower vertical angle first ($\Delta t = 30$ ps), followed by broadening to both sides and shifting to the lower side ($\Delta t = 60$ ps). At a relatively large delay time of $\Delta t = 150$ ps, the peak becomes slightly narrower but remains broadened toward the lower vertical angle. The change of peak position is more clearly seen in raw data of Figs. 2(a)-2(d), in which the horizontal white-dashed lines indicate the peak position before the arrival of pump. On the other hand, the peak position is not clearly traced in difference images because they are also influenced by the reduction of peak intensity or broadening of the peak profile. These dynamics reflect the significant lattice compressions and expansions along the c axis in the ultrafast time scale, which is described below in more detail.

To quantitatively evaluate the lattice dynamics along the c axis, we examined the vertical profile intersecting the highest point of the peak, shown as the white-dashed line in Fig. 2(b). The red markers in Fig. 3(a) indicate the vertical profile of the (008) Bragg peak at $\Delta t = 30$ ps. Note that the peak is

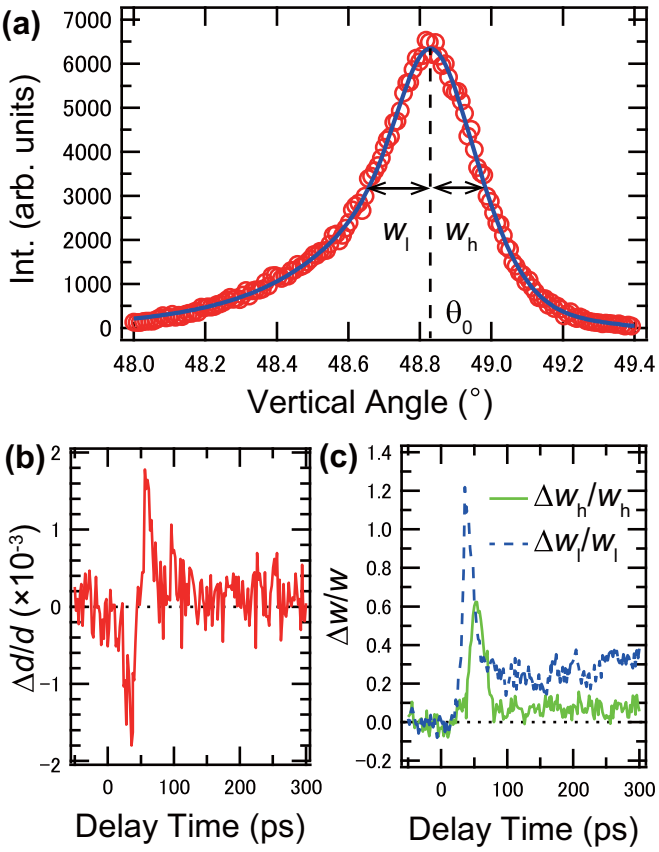

FIG. 3. (a) The profile along the white-dashed line in Fig. 2(b) for the diffraction image of the (008) Bragg peak at Δt = 30 ps. Fitting was performed using a split pseudo-Voigt function expressed by Eq. (3). (b), (c) Dynamics of the c axis length and the fitting parameters of w_h and w_l corresponding to the peak widths at the higher and lower angle sides, respectively. All of them are shown as ratio of change.

asymmetric between lower and higher vertical angles with respect to the highest point of the peak. To extract the center angle of the peak, which is defined as the highest point of the asymmetric peak, and the half-width at the half maximum (HWHM) at the lower and higher angles, we fit the data by the split pseudo-Voigt function [47], which is given as follows:

$$I = I_0 + A\Bigg[\Theta(\theta-\theta_0)\Bigg(\eta_h\frac{w_h^2}{(\theta-\theta_0)^2+w_h^2} + (1-\eta_h)\exp\left(-\ln(2)\left(\frac{\theta-\theta_0}{w_h}\right)^2\right)\Bigg) + \Theta(\theta_0-\theta)\Bigg(\eta_l\frac{w_l^2}{(\theta-\theta_0)^2+w_l^2} + (1-\eta_l)\exp\left(-\ln(2)\left(\frac{\theta-\theta_0}{w_l}\right)^2\right)\Bigg)\Bigg], \quad (3)$$

where I_0 and A correspond to the background level and peak amplitude, respectively, and $\eta_l(1-\eta_l)$ and $\eta_h(1-\eta_h)$ are the weights of the Lorentzian (Gaussian) functions at the lower and higher angles, respectively, with values of $0 < \eta_l, \eta_h < 1$. It should be mentioned that by using this function we can obtain the center angles and widths at both the lower and the higher angles even if the Bragg peak profiles appearing in this work become asymmetrically distorted and substantially change with delay time. We have also set the widths at the lower and higher angles given by w_l and w_h, respectively, as HWHMs irrespective of the values of η_l and η_h, which also change with delay time. The fitting result is shown by the blue solid line in Fig. 3(a).

From the fitting results, we can obtain the time-dependent θ_0, w_h, and w_l. We can also deduce the c axis length change as $\Delta d/d$ from the time-dependent θ_0 using the relationship in Eq. (2). Each parameter is plotted in Figs. 3(b) and 3(c) as a function of the delay time. Because the hard x-ray pulse probes the entire depth from the surface, the obtained values of $\Delta d/d$, w_h, and w_l are averaged along the c axis. Thus, from the obtained values of w_h and w_l, we can gain insights into the inhomogeneity in the lattice spacing along the c axis. A larger $w_{h/l}$ corresponds to a more inhomogeneous lattice spacing distributed to smaller/larger d values. From Fig. 3(b), $\Delta d/d$ shows an interesting behavior; e.g., $\Delta d/d$ first decreases at $\Delta t \sim 30$ ps and then increases at $\Delta t \sim 60$ ps, followed by strong damping to $\Delta d/d \sim 0$. These dynamics show that after photoexcitation, the lattice contracts along the c axis first and then expands. By observing the dynamic behaviors of the peak widths $\Delta w_h/w_h$ and $\Delta w_l/w_l$ in Fig. 3(c), w_l first increases, followed by an increase in w_h. This behavior is most likely the result of the shift to higher angles followed by the shift to lower angles of the center position θ_0 by comparing the delay times at which the $\Delta w_h/w_h$ and $\Delta w_l/w_l$ reach the maximum values. More specifically, the situation at $\Delta t \sim 30$ ps seems to be corresponding to the lattice profile where the contraction only occurs near the surface, while the lattice spacings apart from the surface do not substantially change. After 100 ps, w_l remains high, which suggests that the distribution of the lattice spacing becomes more inhomogeneous for larger d values.

Focusing on the behavior of $\Delta d/d$, we performed pump-fluence-dependent measurements for multiple Bragg peaks. Figure 4 shows a summary of the changes in the lattice spacing $\Delta d/d$ for the contraction at $\Delta t \sim 30$ ps and the expansion at $\Delta t \sim 60$ ps. The full results for the fluence-dependent $\Delta d/d$ results are shown in Supplemental Figure S1 [48]. Notably, the contraction and expansion occur at a similar delay time regardless of the pump fluence or Bragg peaks. As can be clearly seen, with increasing pump fluence, both contraction and expansion become more pronounced. We can further deduce the normal stress along the c axis, $\sigma_{\rm def}$, induced by lattice deformation, $\Delta d/d$, using the following relationship:

$$\sigma_{\rm def} = E\frac{\Delta d}{d}, \quad (4)$$

where $E = 73$ GPa is the Young modulus [49].

Regarding the photo-induced superconductivity, the previous report employs the infrared pulses of a few mJ/cm^2 [50] while our work reached $10-30$ mJ/cm^2. In terms of the heating effect, the higher pump fluence is an obstacle to achieving the photo-induced order. However, strong pulse excitation is necessary to observe the change of Bragg peak because the penetration depth for x-ray is larger than the sample thickness, and the observed peak is averaged along the depth direction.

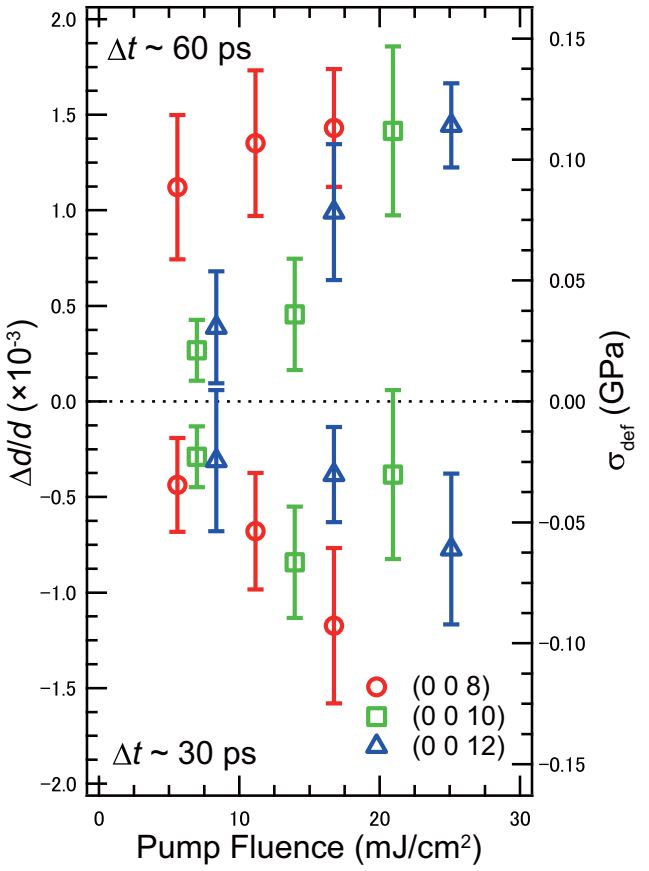

FIG. 4. A summary of the c axis length contraction ($\Delta t \sim 30$ ps) and expansion ($\Delta t \sim 60$ ps) for multiple Bragg peaks as a function of the pump fluence. The normal stress along the c axis is obtained from $\Delta d/d$ using the relationship in Eq. (4).

For the time scale, the reported photo-induced superconductivities in cuprates are achieved within a few ps [50,51] while our observation is on the order of 10–100 ps. However, the long lifetime of iron-based superconductors of $Fe(Te_{1-x}Se_x)$ after photoexcitation was reported [27,52] owing to the indirect semimetalic band structure which is a common profile in iron-based superconductors. Thus, this material system may be favorable for photo-induced change in the relatively longer time scale.

As previously mentioned, the obtained $\Delta d/d$ is averaged in the depth direction. The obtained normal stress along the c axis is also averaged, and we cannot determine the distribution of σ along the depth direction. In addition, the observed dynamics of the c axis length change do not simply show monotonic behavior, and the behavior is rather complicated; e.g., it first contracts and then expands. These complex behaviors mask our understanding of what happens temporally and spatially after photoexcitation.

IV. SIMULATIONS

A. Overall

To gain insights into the mechanism of the observed lattice dynamics induced by photoexcitation, we performed simulations based on the combined models, consisting of a two-temperature model and an ultrafast thermoelasticity model. The pioneering work for the dynamics of strain and stress can be found in 1980s [53]. Since then, the above models have been particularly employed in the field of laser processing of metals [54–63]. We applied the slightly modified models to $BaFe_2As_2$ and compared the results with the experimental results.

TABLE I. Parameters for the two-temperature model.

C_e	$760\,T_e$ (J/m^{3}K)	[67]
C_l	2.0×10^6 (J/m^{3}K)	[67]
K_e	$1.6 \times 10^{-3}\,T_e$ (W/mK)	[68]

B. Two-temperature model

First, we calculated the depth and temporal distributions of the electron (T_e) and lattice (T_l) temperatures by solving two-temperature models [64–66] as functions of time (t) and depth (x), as shown below:

$$C_e \frac{\partial T_e}{\partial t} = -\frac{\partial}{\partial x}\left(K_e \frac{\partial T_e}{\partial x}\right) - G(T_e - T_l) + S(x,t), \quad (5)$$

$$C_l \frac{\partial T_l}{\partial t} = G(T_e - T_l), \quad (6)$$

where C_e and C_l are the specific heats of the electron and lattice systems [67], K_e is the electron thermal conductivity, and G is the coupling constant between the electron and lattice systems. Each value of the parameters is shown in Table I. K_e is estimated from the electrical conductivity along the c axis using the Wiedemann–Franz law, where we set the resistivity along the c axis, ρ_c (300 K), as 1500 $\mu\Omega$ cm [68]. G is related to the Eliashberg electron-phonon coupling function $\lambda\langle\omega^2\rangle$ as $G = 3\lambda\langle\omega^2\rangle/\pi k_B$ [64]. We set $\lambda\langle\omega^2\rangle$ as 30 meV^2, which is consistent with a previous report measured by time-resolved ARPES [66]. $S(x,t)$ is the depth and temporal profile of the laser pulses used, which is written as follows:

$$S(x,t) = J_0\sqrt{\frac{\ln 2}{\pi}}\frac{1-R}{t_p x_d}\exp\left[-\ln(2)\left(\frac{t}{t_p}\right)^2 - \frac{x}{x_d}\right], \quad (7)$$

where $J_0 = 16\,\mathrm{mJ/cm^2}$ is the pump fluence, $R = 0.5$ is the reflectivity for a pump wavelength of 800 nm [69], $t_p = 13.5$ fs is the time duration of the pump laser corresponding to 27 fs in full width at half maximum, and $x_d = 30$ nm is the penetration depth for the pump wavelength [31,70].

It should be mentioned here that most of the previous works for ultrafast dynamics in iron-based superconductors perform two- or three-temperature models without considering the depth profiles. In this work, we performed it including depth profile by solving a set of diffusion equations, by which we can reach the understanding of observed lattice dynamics. We should also mention the other degrees which play important roles in an iron-based superconductor. One of them is a nematic order in this system. However, our measurements are performed at room temperature, which is much higher than the nematic phase-transition temperature of ~170 K [16]. We have thus neglected this effect in the model. Regarding the time scale of the simulation, some previous works report the relatively shorter time of a few ps is needed to

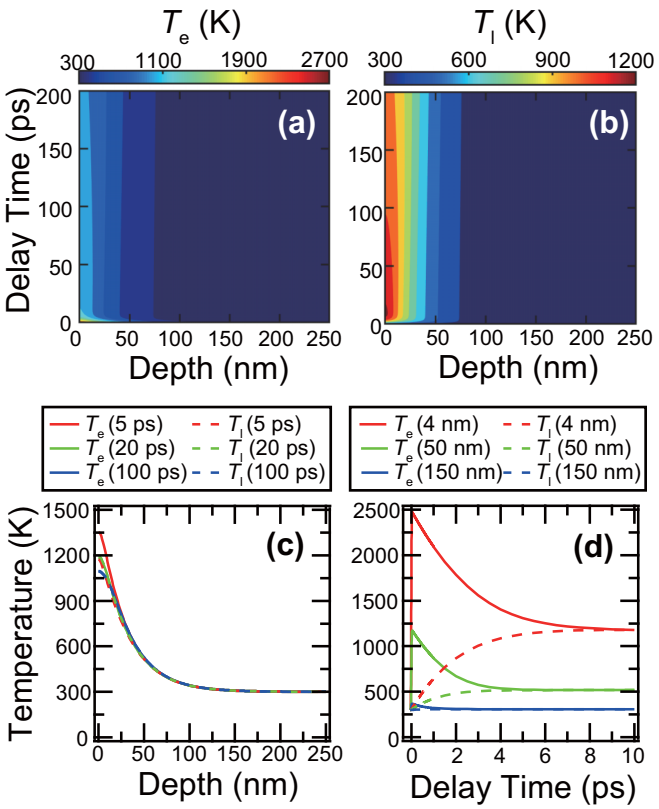

FIG. 5. (a), (b) Calculation results for the depth and temporal distributions of the electron (T_e) and lattice (T_l) temperatures based on the two-temperature model. (c) Spatial distributions of T_e and T_l at several fixed delay time points. The upper, middle, and lower plots at the depth of 0 nm correspond to 5, 20, and 100 ps, respectively. (d) Temporal distributions of T_e and T_l at several fixed depth points. The upper, middle, and lower plots at the delay time of 10 ps correspond to 4, 50, and 150 ps, respectively.

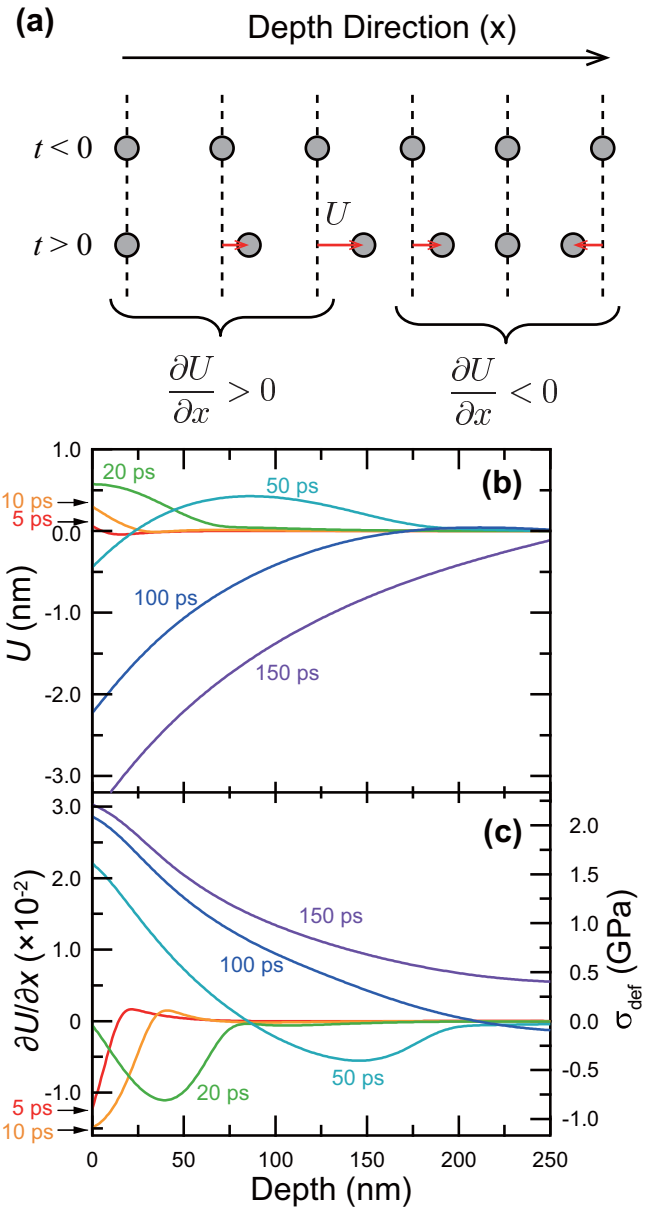

FIG. 6. (a) Schematic diagram of the ultrafast thermoelasticity model. The top configuration corresponds to the equilibrium position, while the bottom one corresponds to the change after photoexcitation. U denotes the displacement from the equilibrium position. (b), (c) Calculation results of U and $\partial U/\partial x$ with the ultrafast thermoelasticity model. The normal stress along the c axis is obtained from $\partial U/\partial x$ using the relationship in Eq. (4).

complete the thermalization between the electron and the phonon systems after the pump fluence of $\sim$1 mJ/cm^2 [66]. In this work, however, we excite with higher pump fluence than 10 mJ/cm^2, and thermalization takes more than 5 ps at a depth of 4 nm as confirmed in Fig. 5(d).

Figures 5(a) and 5(b) show the calculation results of the depth and temporal distributions of T_e and T_l, respectively. As can be clearly seen, T_e and T_l exhibit significantly different behaviors. To understand these behaviors in more detail, we show the depth and temporal distributions of T_e and T_l at several fixed points of delay time and depth in Figs. 5(c) and 5(d), respectively. From the depth profile shown in Fig. 5(c), T_e and T_l significantly increase near the surface, whereas they do not noticeably increase in regions far from the surface. As discussed later, the depth distribution of T_e generates a blast force that triggers the initial lattice contractions. From the temporal profile shown in Fig. 5(d), T_e immediately increases at $\Delta t \sim 0$ ps, followed by a relatively slow decrease in T_e and an increase in T_l occurring at $\Delta t = 0$–8 ps. After 8 ps, T_e and T_l reach the same value, and both gradually decrease to 300 K. Notably, T_e and T_l still remain around 1000 K near the surface even at 100 ps, as shown in Fig 5(c). This behavior is due to the relatively small value of the electron thermal conductivity used in the simulation, which is estimated by assuming the Wiedemann–Franz law with a small electric conductivity along the c axis. We will briefly revisit this counterintuitive issue later using different values for K_e.

C. Ultrafast thermoelasticity model

Next, we discuss how the dynamical changes in the depth and temporal distributions of T_e and T_l induce lattice dynamics. We performed calculations based on the ultrafast thermoelasticity model [54,56,60]. Figure 6(a) schematically

TABLE II. Parameters for the ultrafast thermoelasticity model.

ρ	6.48×10^3 (kg/m^3)	[71]
E	73 (GPa)	[49]
α	2.5×10^{-5} (K^{-1})	[72]

details the parameters used in the equations. They are expressed as follows:

$$\rho \frac{\partial^2 U}{\partial t^2} = \frac{\partial \sigma_{\rm tot}}{\partial x} + \Lambda \frac{\partial}{\partial x}(T_e^2) - \gamma \frac{\partial U}{\partial t} \tag{8}$$

$$\sigma_{\rm tot} = E\left(\frac{\partial U}{\partial x} - \alpha(T_l - T_0)\right). \tag{9}$$

U is the displacement from the equilibrium position at 300 K, ρ is the mass density [71], Λ is the blast force parameter, and γ is the phenomenological damping constant; $\sigma_{\rm tot}$ is the normal stress along the c axis, where α is the thermal expansion coefficient [72]. Both the front and the back of the crystal are allowed to move freely as the boundary condition. T_0 is the room temperature (300 K). As shown in Eq. (9), $\sigma_{\rm tot}$ comprises two terms, where the first term is due to the lattice deformation corresponding to Eq. (4) and the second term denotes the thermal expansion. The reported value of each parameter is shown in Table II. To obtain the best agreement with the experimental results shown later, we set $\Lambda = 600$ J/m^{3}K^2, and $\gamma = 5.0 \times 10^{14}$ kg/m^{3}s; $\Delta d/d$ corresponds to $\partial U/\partial x$. The condition for expansion is $\partial U/\partial x > 0$, whereas contraction occurs when $\partial U/\partial x < 0$, as shown in Fig. 6(a).

Figures 6(b) and 6(c) show the calculation results of the depth distribution of U and $\partial U/\partial x$ at several fixed delay time points. As can be clearly seen, the c axis length first contracts ($\partial U/\partial x < 0$) near the surface at $\Delta t = 5$–20 ps because of the blast force, as previously reported for metallic crystals with a thickness of several tens to hundreds of nanometers [61,62], and then expands at $\Delta t = 50$–150 ps because of the distribution of T_l. The elastic property is also seen in the initial dynamics of $\partial U/\partial x$ at $\Delta t = 10$–50 ps as the minimum position propagates along the depth direction at the sound velocity $\sqrt{E/\rho} = 3.4$ nm/ps.

D. Depth integration

For comparison with the experimental results, we employed integrals along the depth direction for the calculation results. We assume that the Bragg peak signal at depth x has a Gaussian profile, the center of which is located at $\partial U(x)/\partial x$ with a width of Δw; Δw was experimentally determined to be 2.2×10^{-3} by taking the HWHM position of the Bragg peak signal before the arrival of the pump as $\Delta w = \Delta d_{\rm HWHM}/d = \sin\theta_0/\sin\theta_{\rm HWHM} - 1$, where $\theta_{\rm HWHM}$ is the angle at the HWHM of the Bragg peak. Consequently, the integral along the depth direction can be calculated as a function of the distribution (w) as follows:

$$I(w) = \int_{x=0}^{x=250nm} W(x) \exp\left(-\ln(2)\left(\frac{w - \frac{\partial U(x)}{\partial x}}{\Delta w}\right)^2\right) dx, \tag{10}$$

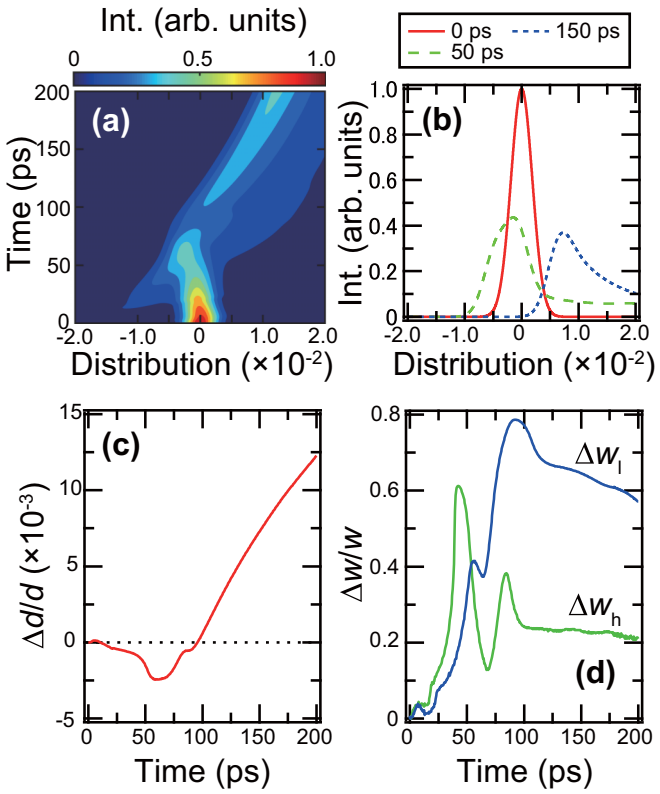

FIG. 7. (a) Calculation results of the (00l) Bragg peak as a function of time. (b) Line profiles for several points of delay time of the (00l) Bragg peak. (c), (d) Calculation results for $\Delta d/d$ and $\Delta w/w$.

where $W(x)$ is the weight function. Because the penetration depth of the x-ray probe pulse is much larger than the film thickness of 250 nm, the weight function is assumed to be independent of x, $W(x) = \text{const}$.

Figure 7(a) shows the time-dependent calculation results of the (00l) Bragg peak as a color plot, and Fig. 7(b) shows the line profile for several delay time points. At $\Delta t = 50$ ps, the peak shifts to a lower value of w, followed by an opposite shift to the higher value of w at $\Delta t = 150$ ps. By tracking the peak value and width, we can observe the dynamical behavior of $\Delta d/d$ and $\Delta w/w$, as shown in Figs. 7(c) and 7(d). To make a comparison with the experimental results more clearly, we define $\Delta w_{h,l}/w$ in Fig. 7(d) as the width of the higher and lower *angle* values, respectively, which are opposite to the distribution of d. Although we cannot reproduce the experimental data perfectly in the simple models used in this work, the simulation results can capture the overall trends well. For example, $\Delta d/d$ first shows a decrease followed by an increase, which captures the experimental behavior shown in Fig. 3(b). Notably, Δw_h and Δw_l exhibit a rapid increase at around 30–50 ps and then relax, as was observed in the experiment. These results confirm that the initial decrease in $\Delta d/d$ is due to the blast force, whereas the later expansion is due to thermal expansion after energy transfer from the electron to the lattice systems. The residual broadening, which is especially apparent in Δw_l for a larger delay time, reflects the inhomogeneous depth distribution of T_l.

E. Follow-up

All parameters listed in Tables I and II are the values reported at room temperature. However, it is not assured that these values can be used in the nonequilibrium states, especially under the condition in which the electron temperature is much higher than the lattice temperature. Among the parameters used in this work, the most uncertain point is the assumption of the Wiedemann–Franz law for the electron thermal conductivity, K_e. Figure 5 shows both T_e and T_l are still in the range of 1000 K near the surface at 100 ps, which is not a trivial situation. To determine how the value of K_e affects the depth and temporal behavior of T_e, T_l, and lattice dynamics, we performed the same simulation using a constant value of $K_e = 50$ W/mK. Calculation results are shown in Supplemental Figs. S2–S4 [48]. We set $\Lambda = 1000$ J/m^{3}K^2, and $\gamma = 5.0 \times 10^{14}$ kg/m^{3}s to obtain the best agreement with the experiment. Note that the overall trend can still be reproduced using $K_e = 50$ W/mK. It is also worth comparing the calculated lattice temperature with the melting point of $BaFe_2As_2$, which was reported to be 1443 K [73]. In case of the maximum pump fluence of 25 mJ/cm^2 in this work, the calculated lattice temperature near the surface at 10 ps would reach above the melting temperature as shown in Supplemental Figure S5 [48]. However, no laser abrasion was confirmed in our experiment. This discrepancy might be ascribed to the nonequilibrium condition, where the lattice temperature only temporarily surpasses the melting temperature.

Although the purpose of the simulation in this work is not to perfectly or quantitatively reproduce the experimental observation but to capture the underlying mechanism of initial contractions followed by expansions, it is worth mentioning other effects that are not considered in the calculations in this work. It is apparent that the presence of a heat bath would result in a more efficient energy reduction from both the electron and the lattice systems. In the calculation, we consider a closed system comprising electrons and lattice systems. Another aspect is the boundary condition. As mentioned in Sec. II, the Method section, the sample was deposited on a MgO substrate; therefore, the effects of the substrate and interface cannot be ignored in the experiment. However, our calculation treats the sample in a free standing condition. More rigorous computations [59,60] might be necessary to perform to understand the time scale or dynamical behaviors of the peak widths, which we did not discuss much in this work. However, our model can successfully capture our central findings, i.e., the initial contraction followed by the expansions in $BaFe_2As_2$, which show the enhancement of superconductivity under physical pressure. To this end, our model is more cost effective for computing than the previous work [59] and allows us to obtain detailed information.

V. DISCUSSION

The immediate increase in the electron temperature and its distribution along the depth direction generate a strong blast force, which results in lattice contraction near the surface. After transferring the energy from the electron to the lattice systems, the gradient in the distribution of T_l along the depth direction leads to the opposite normal stress that drives the lattice to expansion. The most interesting aspect is the normal stress instantaneously generated after photoexcitation at $\Delta t \sim 50$ ps, as shown in Fig. 7(c), which was observed experimentally at $\Delta t \sim 30$ ps, as shown in Figs. 3(b) and 4. By raising only the electron temperature, which can be realized in a nonequilibrium process, a blast force is generated to produce uniaxial stress that is especially enhanced near the surface. Thus, our work demonstrates that photoexcitation can temporally induce strong uniaxial stress on an ultrafast time scale.

Regarding superconductivity, high pressure is a very important tool for enhancing superconductivity, which has been widely demonstrated in numerous superconducting materials, including nonconventional [74] and high-temperature superconductors [75]. Based on the investigation of the roles of the lattice and electrons under high pressure, we can gain important knowledge for designing materials exhibiting higher T_c. Recently, it was shown that superconductivity can be achieved in lanthanum superhydrides above 260 K at 180–200 GPa [76], which is in the vicinity of room temperature. More recently, room-temperature (287 K) superconductivity has also been reported in a carbonaceous sulfur hydride at 267 GPa [77]. Dramatic enhancement of superconductivity has also been demonstrated in iron-based superconductors [25,78,79]. Ultrafast manipulation of high stress in confined spaces can be an alternative route to design exotic electronic and lattice structures that cannot be achieved under static conditions and might be applied to enhance superconductivity.

Although all reports achieved these results under hydrostatic pressure, note that uniaxial stress or anisotropic strain can also considerably control the physical properties of strongly correlated materials. For high-T_c cuprate superconductors, by applying a uniaxial stress, a higher transition temperature can be induced, and the sensitivity is found to be highly anisotropic [80,81]. For iron-based superconductors, anisotropic strain is used to tune the structural and nematic transition temperatures, which has revealed the importance of nematic fluctuation for the emergence of superconductivity [82,83]. In addition to the high-T_c superconductivity, a model unconventional superconductor, Sr_2RuO_4, was found to exhibit a significantly sensitive response for the rise of T_c to the application of the uniaxial strain [84,85]. In this respect, our work presents a new platform for studying the uniaxial strain effect that can be achieved on an ultrafast time scale. The combined ultrafast measurements using TARPES for superconducting gap in addition to TRXRD measurements will enable us to further elucidate the dynamical physical properties.

VI. CONCLUSION

In summary, we investigated the photoexcited lattice dynamics in $BaFe_2As_2$ by TRXRD using XFEL at SACLA. We observed a significant lattice contraction which occurred at an ultrafast time scale of $\Delta t \sim 30$ ps because of a blast force.

Our findings can pave the way for the external stimuli to investigate superconducting materials.

ACKNOWLEDGMENTS

We acknowledge K. Tamasaku for valuable discussions and comments. This work was supported by Grants-in-Aid for Scientific Research (KAKENHI) (Grants No. JP18K13498, No. JP19H00659, No. JP19H01818, and No. JP19H00651) from the Japan Society for the Promotion of Science (JSPS), by JSPS KAKENHI on Innovative Areas "Quantum Liquid Crystals" (Grants No. JP19H05824 and No. JP19H05826), and the Quantum Leap Flagship Program (Q-LEAP) (Grant No. JPMXS0118068681) from the Ministry of Education, Culture, Sports, Science, and Technology (MEXT). This experiment was performed at BL3 of SACLA with the approval of the Japan Synchrotron Radiation Research Institute (JASRI) (Proposal No. 2017B8067). The authors acknowledge the support from members of the SACLA facility. S.I. acknowledges the JSPS Research Fellowship for Young Scientists (DC2) and financial support from JSPS through the Program for Leading Graduate School (Materials Education Program for the Future Leaders in Research, Industry, and Technology). H.Hi. and H.Ho. were supported by the Ministry of Education, Culture, Sports, Science, and Technology (MEXT) through the Element Strategy Initiative to Form Core Research Center (Grant No. JPMXP0112101001).

[1] D. N. Basov, R. D. Averitt, and D. Hsieh, Towards properties on demand in quantum materials, Nat. Mater. **16**, 1077 (2017).

[2] H. Ichikawa, S. Nozawa, T. Sato, A. Tomita, K. Ichiyanagi, M. Chollet, L. Guerin, N. Dean, A. Cavalleri, S. Adachi *et al.*, Transient photoinduced 'hidden' phase in a manganite, Nat. Mater. **10**, 101 (2011).

[3] A. Zong, A. Kogar, Y.-Q. Bie, T. Rohwer, C. Lee, E. Baldini, E. Ergeen, M. B. Yilmaz, B. Freelon, E. J. Sie *et al.*, Evidence for topological defects in a photoinduced phase transition, Nat. Phys. **15**, 27 (2019).

[4] A. Kogar, A. Zong, P. E. Dolgirev, X. Shen, J. Straquadine, Y.-Q. Bie, X. Wang, T. Rohwer, I.-C. Tung, Y. Yang *et al.*, Light-induced charge density wave in $LaTe_3$, Nat. Phys. **16**, 159 (2019).

[5] D. Fausti, R. I. Tobey, N. Dean, S. Kaiser, A. Dienst, M. C. Hoffmann, S. Pyon, T. Takayama, H. Takagi, and A. Cavalleri, Light-induced superconductivity in a stripe-ordered cuprate, Science **331**, 189 (2011).

[6] A. Cavalleri, Photo-induced superconductivity, Contemp. Phys. **59**, 31 (2018).

[7] R. Mankowsky, A. Subedi, M. Först, S. O. Mariager, M. Chollet, H. T. Lemke, J. S. Robinson, J. M. Glownia, M. P. Minitti, A. Frano *et al.*, Nonlinear lattice dynamics as a basis for enhanced superconductivity in $YBa_2Cu_3O_{6.5}$, Nature (London) **516**, 71 (2014).

[8] H. J. Zeiger, J. Vidal, T. K. Cheng, E. P. Ippen, G. Dresselhaus, and M. S. Dresselhaus, Theory for Displacive Excitation of Coherent Phonons, Phys. Rev. B **45**, 768 (1992).

[9] K. Kuroki, S. Onari, R. Arita, H. Usui, Y. Tanaka, H. Kontani, and H. Aoki, Unconventional Pairing Originating from the Disconnected Fermi Surfaces of Superconducting $LaFeAsO_{1-x}F_x$, Phys. Rev. Lett. **101**, 087004 (2008).

[10] I. I. Mazin, D. J. Singh, M. D. Johannes, and M. H. Du, Unconventional Superconductivity with a Sign Reversal in the Order Parameter of $LaFeAsO_{1-x}F_x$, Phys. Rev. Lett. **101**, 057003 (2008).

[11] T. Hanaguri, S. Niitaka, K. Kuroki, and H. Takagi, Unconventional s-wave superconductivity in Fe(Se, Te), Science **328**, 474 (2010).

[12] A. D. Christianson, E. A. Goremychkin, R. Osborn, S. Rosenkranz, M. D. Lumsden, C. D. Malliakas, I. S. Todorov, H. Claus, D. Y. Chung, M. G. Kanatzidis *et al.*, Unconventional superconductivity in $Ba_{0.6}K_{0.4}Fe_2As_2$ from inelastic neutron scattering, Nature (London) **456**, 930 (2008).

[13] K. Okazaki, Y. Ota, Y. Kotani, W. Malaeb, Y. Ishida, T. Shimojima, T. Kiss, S. Watanabe, C.-T. Chen, K. Kihou *et al.*, Octet-line node structure of superconducting order parameter in KFe_2As_2, Science **337**, 1314 (2012).

[14] T. Hashimoto, Y. Ota, H. Q. Yamamoto, Y. Suzuki, T. Shimojima, S. Watanabe, C. Chen, S. Kasahara, Y. Matsuda, T. Shibauchi *et al.*, Superconducting gap anisotropy sensitive to nematic domains in FeSe, Nat. Commun. **9**, 282 (2018).

[15] J.-H. Chu, H.-H. Kuo, J. G. Analytis, and I. R. Fisher, Divergent nematic susceptibility in an iron arsenide superconductor, Science **337**, 710 (2012).

[16] S. Kasahara, H. J. Shi, K. Hashimoto, S. Tonegawa, Y. Mizukami, T. Shibauchi, K. Sugimoto, T. Fukuda, T. Terashima, A. H. Nevidomskyy *et al.*, Electronic nematicity above the structural and superconducting transition in $BaFe_2(As_{1-x}Px)_2$, Nature (London) **486**, 382 (2012).

[17] T. Shimojima, Y. Suzuki, T. Sonobe, A. Nakamura, M. Sakano, J. Omachi, K. Yoshioka, M. Kuwata-Gonokami, K. Ono, H. Kumigashira *et al.*, Lifting of xz/yz orbital degeneracy at the structural transition in detwinned FeSe, Phys. Rev. B **90**, 121111(R) (2014).

[18] K. Okazaki, Y. Ito, Y. Ota, Y. Kotani, T. Shimojima, T. Kiss, S. Watanabe, C.-T. Chen, S. Niitaka, T. Hanaguri *et al.*, Superconductivity in an electron band just above the Fermi level: Possible route to BCS-BEC superconductivity, Sci. Rep. **4**, 4109 (2014).

[19] S. Rinott, K. B. Chashka, A. Ribak, E. D. L. Rienks, A. Taleb-Ibrahimi, P. L. Fevre, F. Bertran, M. Randeria, and A. Kanigel, Tuning across the BCS-BEC crossover in the multiband superconductor $Fe_{1+y}Se_xTe_{1-x}$: An angle-resolved photoemission study, Sci. Adv. **3**, e1602372 (2017).

[20] T. Hanaguri, S. Kasahara, J. Böker, I. Eremin, T. Shibauchi, and Y. Matsuda, Quantum Vortex Core and Missing Pseudogap in the Multiband BCS-BEC Crossover Superconductor FeSe, Phys. Rev. Lett. **122**, 077001 (2019).

[21] T. Hashimoto, Y. Ota, A. Tsuzuki, T. Nagashima, A. Fukushima, S. Kasahara, Y. Matsuda, K. Matsuura, Y. Mizukami, T. Shibauchi, S. Shin, and K. Okazaki, Bose-Einstein condensation superconductivity induced by disappearance of the nematic state, Sci. Adv. **6**, eabb9052 (2020).

[22] M. Burrard-Lucas, D. G. Free, S. J. Sedlmaier, J. D. Wright, S. J. Cassidy, Y. Hara, A. J. Corkett, T. Lancaster, P. J. Baker, S. J. Blundell *et al.*, Enhancement of the superconducting transition temperature of FeSe by intercalation of a molecular spacer layer, Nat. Mater. **12**, 15 (2013).

[23] S. He, J. He, W. Zhang, L. Zhao, D. Liu, X. Liu, D. Mou, Y.-B. Ou, Q.-Y. Wang, Z. Li *et al.*, Phase diagram and electronic indication of high-temperature superconductivity at 65K in single-layer FeSe films, Nat. Mater. **12**, 605 (2013).

[24] S. Kasahara, T. Shibauchi, K. Hashimoto, K. Ikada, S. Tonegawa, R. Okazaki, H. Shishido, H. Ikeda, H. Takeya, K. Hirata *et al.*, Evolution from non-Fermi- to Fermi-liquid transport via isovalent doping in $BaFe_2(As_{1-x}P_x)_2$ superconductors, Phys. Rev. B **81**, 184519 (2010).

[25] E. Colombier, S. L. Bud'ko, N. Ni, and P. C. Canfield, Complete pressure-dependent phase diagrams for $SrFe_2As_2$ and $BaFe_2As_2$, Phys. Rev. B **79**, 224518 (2009).

[26] K. Okazaki, H. Suzuki, T. Suzuki, T. Yamamoto, T. Someya, Y. Ogawa, M. Okada, M. Fujisawa, T. Kanai, N. Ishii *et al.*, Antiphase Fermi-surface modulations accompanying displacement excitation in a parent compound of iron-based superconductors, Phys. Rev. B **97**, 121107(R) (2018).

[27] T. Suzuki, T. Someya, T. Hashimoto, S. Michimae, M. Watanabe, M. Fujisawa, T. Kanai, N. Ishii, J. Itatani, S. Kasahara *et al.*, Photoinduced possible superconducting state with long-lived disproportionate band filling in FeSe, Commun. Phys. **2**, 115 (2019).

[28] S. Yang, J. A. Sobota, D. Leuenberger, A. F. Kemper, J. J. Lee, F. T. Schmitt, W. Li, R. G. Moore, P. S. Kirchmann, and Z.-X. Shen, Thickness-dependent coherent phonon frequency in ultrathin $FeSe/SrTiO_3$ films, Nano Lett. **15**, 4150 (2015).

[29] S. Gerber, S.-L. Yang, D. Zhu, H. Soifer, J. A. Sobota, S. Rebec, J. J. Lee, T. Jia, B. Moritz, C. Jia *et al.*, Femtosecond electron-phonon lock-in by photoemission and x-ray free-electron laser, Science **357**, 71 (2017).

[30] K. W. Kim, A. Pashkin, H. Schäfer, M. Beyer, M. Porer, T. Wolf, C. Bernhard, J. Demsar, R. Huber, and A. Leitenstorfer, Ultrafast transient generation of spin-density-wave order in the normal state of $BaFe_2As_2$ driven by coherent lattice vibrations, Nat. Mater. **11**, 497 (2012).

[31] L. X. Yang, G. Rohde, T. Rohwer, A. Stange, K. Hanff, C. Sohrt, L. Rettig, R. Cortés, F. Chen, D. L. Feng *et al.*, Ultrafast Modulation of the Chemical Potential in $BaFe_2As_2$ by Coherent Phonons, Phys. Rev. Lett. **112**, 207001 (2014).

[32] L. Rettig, S. O. Mariager, A. Ferrer, S. Grübel, J. A. Johnson, J. Rittmann, T. Wolf, S. L. Johnson, G. Ingold, P. Beaud *et al.*, Ultrafast Structural Dynamics of the Fe-Pnictide Parent Compound $BaFe_2As_2$, Phys. Rev. Lett. **114**, 067402 (2015).

[33] L. Rettig, S. O. Mariager, A. Ferrer, S. Grübel, J. A. Johnson, J. Rittmann, T. Wolf, S. L. Johnson, G. Ingold, P. Beaud *et al.*, Ultrafast structural dynamics of the orthorhombic distortion in the Fe-pnictide parent compound $BaFe_2As_2$, Struct. Dyn. **3**, 023611 (2016).

[34] P. Beaud, A. Caviezel, S. O. Mariager, L. Rettig, G. Ingold, C. Dornes, S-W. Huang, J. A. Johnson, M. Radovic, T. Huber *et al.*, A time-dependent order parameter for ultrafast photoinduced phase transitions, Nat. Mater. **13**, 923 (2014).

[35] S. de Jong, R. Kukreja, C. Trabant, N. Pontius, C. F. Chang, T. Kachel, M. Beye, F. Sorgenfrei, C. H. Back, B. Bräuer *et al.*, Speed limit of the insulator-metal transition in magnetite, Nat. Mater. **12**, 882 (2013).

[36] S. Gerber, K. W. Kim, Y. Zhang, D. Zhu, N. Plonka, M. Yi, G. L. Dakovski, D. Leuenberger, P. S. Kirchmann, R. G. Moore *et al.*, Direct characterization of photoinduced lattice dynamics in $BaFe_2As_2$, Nat. Commun. **6**, 7377 (2015).

[37] T. Ishikawa, H. Aoyagi, T. Asaka, Y. Asano, N. Azumi, T. Bizen, H. Ego, K. Fukami, T. Fukui, Y. Furukawa *et al.*, A compact X-ray free-electron laser emitting in the sub-ångström region, Nat. Photonics **6**, 540 (2012).

[38] C. v. Korff Schmising, A. Harpoeth, N. Zhavoronkov, Z. Ansari, C. Aku-Leh, M. Woerner, T. Elsaesser, M. Bargheer, M. Schmidbauer, I. Vrejoiu *et al.*, Ultrafast magnetostriction and phonon-mediated stress in a photoexcited ferromagnet, Phys. Rev. B **78**, 060404(R) (2008).

[39] M. Yabashi, H. Tanaka, and T. Ishikawa, Overview of the SACLA Facility, J. Synchrotron Radiat. **22**, 477 (2015).

[40] K. Tono, T. Hara, M. Yabashi, and H. Tanaka, Multiple-beamline operation of SACLA, J. Synchrotron Radiat. **26**, 595 (2019).

[41] T. Katayama, S. Owada, T. Togashi, K. Ogawa, P. Karvinen, I. Vartiainen, A. Eronen, C. David, T. Sato, K. Nakajima *et al.*, A beam branching method for timing and spectral characterization of hard x-ray free-electron lasers, Struct. Dyn. **3**, 034301 (2016).

[42] K. Nakajima, Y. Joti, T. Katayama, S. Owada, T. Togashi, T. Abe, T. Kameshima, K. Okada, T. Sugimoto, M. Yamaga *et al.*, Software for the data analysis of the arrival-timing monitor at SACLA, J. Synchrotron Radiat. **25**, 592 (2018).

[43] K. Yamamoto, Y. Kubota, M. Suzuki, Y. Hirata, K. Carva, M. Berritta, K. Takubo, Y. Uemura, R. Fukaya, K. Tanaka *et al.*, Ultrafast demagnetization of Pt magnetic moment in L10 − FePt probed by magnetic circular dichroism at a hard X-ray free electron laser, New J. Phys. **21**, 123010 (2019).

[44] T. Kameshima, S. Ono, T. Kudo, K. Ozaki, Y. Kirihara, K. Kobayashi, Y. Inubushi, M. Yabashi, T. Horigome, A. Holland, K. Holland, D. Burt, H. Murao, and T. Hatsui, Development of an X-ray pixel detector with multi-port charge-coupled device for X-ray free-electron laser experiments, Rev. Sci. Instrum. **85**, 033110 (2014).

[45] H. Sato, H. Hiramatsu, T. Kamiya, and H. Hosono, High critical-current density with less anisotropy in $BaFe_2(As, P)_2$ epitaxial thin film, Appl. Phys. Lett. **104**, 182603 (2014).

[46] T. Miyake, K. Nakamura, R. Arita, and M. Imada, Comparison of Ab initio low-energy models for LaFePO, LaFeAsO, $BaFe_2As_2$, LiFeAs, FeSe, and FeTe: Electron correlation and covalency, J. Phys. Soc. Jpn. **79**, 044705 (2010).

[47] H. Toraya, Array-type universal profile function for powder pattern fitting, J. Appl. Crystallogr. **23**, 485 (1990).

[48] See Supplemental Material at http://link.aps.org/supplemental/10.1103/PhysRevResearch.3.033222 for the full results for the fluence-dependent $\Delta d/d$ and simulation results with using $K_e = 50\,\mathrm{W/mK}$ and $J_0 = 25\,\mathrm{mJ/cm^2}$.

[49] C. Fujii, S. Simayi, K. Sakano, C. Sasaki, M. Nakamura, Y. Nakanishi, K. Kihou, M. Nakajima, C.-H. Lee, A. Iyo *et al.*, Anisotropic Grüneisen parameter and diverse order parameter fluctuations in iron-based superconductor $Ba(Fe_{1-x}Co_x)_2As_2$, J. Phys. Soc. Jpn. **87**, 074710 (2018).

[50] E. Casandruc, D. Nicoletti, S. Rajasekaran, Y. Laplace, V. Khanna, G. D. Gu, J. P. Hill, and A. Cavalleri, Wavelength-dependent optical enhancement of superconducting interlayer coupling in $La_{1.885}Ba_{0.115}CuO_4$, Phys. Rev. B **91**, 174502 (2015).

[51] S. Kaiser, C. R. Hunt, D. Nicoletti, W. Hu, I. Gierz, H. Y. Liu, M. Le Tacon, T. Loew, D. Haug, B. Keimer, and A. Cavalleri, Optically induced coherent transport far above T_c in underdoped $YBa_2Cu_3O_{6+\delta}$, Phys. Rev. B **89**, 184516 (2014).

[52] L. X. Yang, G. Rohde, Y. J. Chen, W. J. Shi, Z. K. Liu, F. Chen, Y. L. Chen, K. Rossnagel, and M. Bauer, Experimental evidence for a metastable state in $Fe(Te_{1-x}Se_x)$ following coherent-phonon excitation, J. Electron Spectrosc. Relat. Phenom. **250**, 147085 (2021).

[53] C. Thomsen, H. T. Grahn, H. J. Maris, and J. Tauc, Surface generation and detection of phonons by picosecond light pulses, Phys. Rev. B **34**, 4129 (1986).

[54] L. A. Falkovsky and E. G. Mishchenko, Electron-lattice kinetics of metals heated by ultrashort laser pulses, J. Exp. Theor. Phys. **88**, 84 (1999).

[55] J. Hohlfeld, S.-S. Wellershoff, J. Güdde, U. Conrad, V. Jähnke, and E. Matthias, Electron and lattice dynamics following optical excitation of metals, Chem. Phys. **251**, 237 (2000).

[56] J. K. Chen, J. E. Beraun, L. E. Grimes, and D. Y. Tzou, Modeling of femtosecond laser-induced non-equilibrium deformation in metal films, Int. J. Solids Struct. **39**, 3199 (2002).

[57] Y. Gan and J. K. Chen, Thermomechanical wave propagation in gold films induced by ultrashort laser pulses, Mech. Mater. **42**, 491 (2010).

[58] J. Chen, W.-K. Chen, J. Tang, and P. M. Rentzepis, Time-resolved structural dynamics of thin metal films heated with femtosecond optical pulses, Proc. Natl. Acad. Sci. USA **108**, 18887 (2011).

[59] D. Schick, M. Herzog, A. Bojahr, W. Leitenberger, A. Hertwig, R. Shayduk, and M. Bargheer, Ultrafast lattice response of photoexcited thin films studied by X-ray diffraction, Struct. Dyn. **1**, 064501 (2014).

[60] Q.-L. Xiong and X.-G. Tian, Thermomechanical interaction in metal films during ultrashort laser heating, Mech. Adv. Mater. Struct. **22**, 548 (2015).

[61] R. Li, O. A. Ashour, J. Chen, H. E. Elsayed-Ali, and P. M. Rentzepis, Femtosecond laser induced structural dynamics and melting of Cu(111) single crystal. An ultrafast time-resolved x-ray diffraction study, J. Appl. Phys. **121**, 055102 (2017).

[62] R. Li, K. Sundqvist, J. Chen, H. E. Elsayed-Ali, J. Zhang, and P. M. Rentzepis, Transient lattice deformations of crystals studied by means of ultrafast time-resolved x-ray and electron diffraction, Struct. Dyn. **5**, 044501 (2018).

[63] T. A. Assefa, Y. Cao, S. Banerjee, S. Kim, D. Kim, H. Lee, S. Kim, J. H. Lee, S.-Y. Park, I. Eom *et al.*, Ultrafast x-ray diffraction study of melt-front dynamics in polycrystalline thin films, Sci. Adv. **6**, eaax2445 (2020).

[64] P. B. Allen, Theory of thermal relaxation of electrons in metals, Phys. Rev. Lett. **59**, 1460 (1987).

[65] L. Perfetti, P. A. Loukakos, M. Lisowski, U. Bovensiepen, H. Eisaki, and M. Wolf, Ultrafast Electron Relaxation in Superconducting $Bi_2Sr_2CaCu_2O_{8+\delta}$ by time-resolved photoelectron spectroscopy, Phys. Rev. Lett. **99**, 197001 (2007).

[66] I. Avigo, R. Cortés, L. Rettig, S. Thirupathaiah, H. S. Jeevan, P. Gegenwart, T. Wolf, M. Ligges, M. Wolf, J. Fink *et al.*, Coherent excitations and electron-phonon coupling in $Ba/EuFe_2As_2$ compounds investigated by femtosecond time- and angle-resolved photoemission spectroscopy, J. Phys.: Condens. Matter. **25**, 094003 (2013).

[67] J. G. Storey, J. W. Loram, J. R. Cooper, Z. Bukowski, and J. Karpinski, Electronic specific heat of $Ba_{1-x}K_xFe_2As_2$ from 2 to 380 K, Phys. Rev. B **88**, 144502 (2013).

[68] M. A. Tanatar, W. E. Straszheim, H. Kim, J. Murphy, N. Spyrison, E. C. Blomberg, K. Cho, J.-Ph. Reid, B. Shen, L. Taillefer *et al.*, Interplane resistivity of underdoped single crystals $(Ba_{1-x}K_x)Fe_2As_2 (0 \leqslant x < 0.34)$, Phys. Rev. B **89**, 144514 (2014).

[69] E. Uykur, T. Kobayashi, W. Hirata, S. Miyasaka, S. Tajima, and C. A. Kuntscher, Optical study of $BaFe_2As_2$ under pressure: Coexistence of spin-density-wave gap and superconductivity, Phys. Rev. B **92**, 245133 (2015).

[70] D. H. Torchinsky, J. W. McIver, D. Hsieh, G. F. Chen, J. L. Luo, N. L. Wang, and N. Gedik, Nonequilibrium quasiparticle relaxation dynamics in single crystals of hole- and electron-doped $BaFe_2As_2$, Phys. Rev. B **84**, 104518 (2011).

[71] M. Rotter, M. Tegel, D. Johrendt, I. Schellenberg, W. Hermes, and R. Pöttgen, Spin-density-wave anomaly at 140 K in the ternary iron arsenide $BaFe_2As_2$, Phys. Rev. B **78**, 020503(R) (2008).

[72] M. S. da Luz, J. J. Neumeier, R. K. Bollinger, A. S. Sefat, M. A. McGuire, R. Jin, B. C. Sales, and D. Mandrus, High-resolution measurements of the thermal expansion of superconducting Co-Doped $BaFe_2As_2$, Phys. Rev. B **79**, 214505 (2009).

[73] R. Morinaga, K. Matan, H. S. Suzuki, and T. J. Sato, Single-crystal growth of the ternary $BaFe_2As_2$ phase using the vertical Bridgman technique, Jpn. J. Appl. Phys. **48**, 013004 (2009).

[74] M. Nicklas, R. Borth, E. Lengyel, P. G. Pagliuso, J. L. Sarrao, V. A. Sidorov, G. Sparn, F. Steglich, and J. D. Thompson, Response of the heavy-Fermion superconductor $CeCoIn_5$ to pressure: Roles of dimensionality and proximity to a quantum-critical point, J. Phys.: Condens. Matter. **13**, L905 (2001).

[75] A. Yamamoto, N. Takeshita, C. Terakura, and Y. Tokura, High pressure effects revisited for the cuprate superconductor family with highest critical temperature, Nat. Commun. **6**, 8990 (2015).

[76] M. Somayazulu, M. Ahart, A. K. Mishra, Z. M. Geballe, M. Baldini, Y. Meng, V. V. Struzhkin, and R. J. Hemley, Evidence for Superconductivity Above 260 K in Lanthanum Superhydride at Megabar Pressures, Phys. Rev. Lett. **122**, 027001 (2019).

[77] E. Snider, N. Dasenbrock-Gammon, R. McBride, M. Debessai, H. Vindana, K. Vencatasamy, K. V. Lawler, A. Salamat, and R. P. Dias, Room-Temperature superconductivity in a carbonaceous sulfur hydride, Nature(London) **586**, 373 (2020).

[78] J. P. Sun, G. Z. Ye, P. Shahi, J.-Q. Yan, K. Matsuura, H. Kontani, G. M. Zhang, Q. Zhou, B. C. Sales, T. Shibauchi *et al.*, High-T_c Superconductivity in FeSe at High Pressure: Dominant Hole Carriers and Enhanced Spin Fluctuations, Phys. Rev. Lett. **118**, 147004 (2017).

[79] K. Matsuura, Y. Mizukami, Y. Rrai, Y. Sugimura, N. Maejima, A. Machida, T. Watanuki, T. Fukuda, T. Yajima, Z. Hiroi *et al.*, Maximizing T_c by tuning nematicity and magnetism in $FeSe_{1-x}S_x$ superconductors, Nat. Commun. **8**, 1143 (2017).

[80] U. Welp, M. Grimsditch, S. Fleshler, W. Nessler, J. Downey, G. W. Crabtree, and J. Guimpel, Effect of Uniaxial Stress on the Superconducting Transition in $YBa_2Cu_3O_7$, Phys. Rev. Lett. **69**, 2130 (1992).

[81] F. Hardy, N. J. Hillier, C. Meingast, D. Colson, Y. Li, N. Barišić, G. Yu, X. Zhao, M. Greven, and J. S. Schilling, Enhancement of the Critical Temperature of $HgBa_2CuO_{4+\delta}$ by Applying Uniaxial and Hydrostatic Pressure: Implications for a Universal Trend in Cuprate Superconductors, Phys. Rev. Lett. **105**, 167002 (2010).

[82] P. Malinowski, Q. Jiang, J. J. Sanchez, J. Mutch, Z. Liu, P. Went, J. Liu, P. J. Ryan, J.-W. Kim, and J.-H. Chu, Suppression of superconductivity by anisotropic strain near a nematic quantum critical point, Nat. Phys. **16**, 1189 (2020).

[83] T. Worasaran, M. S. Ikeda, J. C. Palmstrom, J. A. W. Straquadine, S. A. Kivelson, and I. R. Fisher, Nematic quantum criticality in an Fe-based superconductor revealed by strain-tuning, Science **372**, 973 (2021).

[84] C. W. Hicks, D. O. Brodsky, E. A. Yelland, A. S. Gibbs, J. A. N. Bruin, M. E. Barber, S. D. Edkins, K. Nishimura, S. Yonezawa, Y. Maeno *et al.*, Strong increase of T_c of Sr_2RuO_4 under both tensile and compressive strain, Science **344**, eaaf9398 (2014).

[85] A. Steppke, L. Zhao, M. E. Barber, T. Scaffidi, F. Jerzembeck, H. Rosner, A. S. Gibbs, Y. Maeno, S. H. Simon, A. P. Mackenzie *et al.*, Strong peak in T_c of Sr_2RuO_4 under uniaxial pressure, Science **355**, eaaf9398 (2017).